

Regulating the catalytic performance of single-atomic-site Ir catalyst for biomass conversion by metal-support interactions

Shubo Tian, Wanbing Gong, Wenxing Chen, Na Lin, Youqi Zhu, Quanchen Feng, Qi Xu, Qiang Fu, Chun Chen, Jun Luo, Wensheng Yan, Huijun Zhao, Dingsheng Wang, and Yadong Li

ACS Catal., Just Accepted Manuscript • DOI: 10.1021/acscatal.9b00322 • Publication Date (Web): 30 Apr 2019

Downloaded from <http://pubs.acs.org> on May 6, 2019

Just Accepted

“Just Accepted” manuscripts have been peer-reviewed and accepted for publication. They are posted online prior to technical editing, formatting for publication and author proofing. The American Chemical Society provides “Just Accepted” as a service to the research community to expedite the dissemination of scientific material as soon as possible after acceptance. “Just Accepted” manuscripts appear in full in PDF format accompanied by an HTML abstract. “Just Accepted” manuscripts have been fully peer reviewed, but should not be considered the official version of record. They are citable by the Digital Object Identifier (DOI®). “Just Accepted” is an optional service offered to authors. Therefore, the “Just Accepted” Web site may not include all articles that will be published in the journal. After a manuscript is technically edited and formatted, it will be removed from the “Just Accepted” Web site and published as an ASAP article. Note that technical editing may introduce minor changes to the manuscript text and/or graphics which could affect content, and all legal disclaimers and ethical guidelines that apply to the journal pertain. ACS cannot be held responsible for errors or consequences arising from the use of information contained in these “Just Accepted” manuscripts.



Regulating the catalytic performance of single-atomic-site Ir catalyst for biomass conversion by metal-support interactions

Shubo Tian^{1†}, Wanbing Gong^{2†}, Wenxing Chen¹, Na Lin³, Youqi Zhu¹, Quanchen Feng¹, Qi Xu¹, Qiang Fu^{4*}, Chun Chen², Jun Luo⁵, Wensheng Yan⁶, Huijun Zhao², Dingsheng Wang^{1*}, and Yadong Li¹

¹Department of Chemistry, Tsinghua University, Beijing 100084, China

²Key Laboratory of Materials Physics, Centre for Environmental and Energy Nanomaterials, Anhui Key Laboratory of Nanomaterials and Nanotechnology, Institute of Solid State Physics, Chinese Academy of Sciences, Hefei 230031, P. R. China

³State Key Laboratory of Crystal Materials, Shandong University, Jinan 250100, China

⁴School of Chemistry and Chemical Engineering, Shandong University, Jinan 250100, China

⁵Center for Electron Microscopy, Tianjin University of Technology, Tianjin 300384, China

⁶National Synchrotron Radiation Laboratory, CAS Center for Excellence in Nanoscience, University of Science and Technology of China, 230029 Hefei, China

ABSTRACT: Metal–support interactions are of significance in clarifying the support–activity relationship over deposited metal catalysts yet rarely considered on single-atomic-site species. Herein, using two single-atomic-site Ir samples supported by the defective metastable phase of titanium dioxide or mesoporous graphitic carbon nitride as the research objects, we demonstrate the effects of metal–support interactions on regulating the geometric and electronic structures of the central Ir species, through which, the catalytic properties are further affected. Experimental results show that the single-atomic-site Ir catalyst supported by the defective metastable phase of titanium dioxide exhibits excellent catalytic performance for the hydrogenation of furfural to furfuryl alcohol, showing outstanding conversion (99%), high selectivity (99%) and good stability that are superior to the mesoporous graphitic carbon nitride supported single-atomic-site Ir sample as well as Ir nanoparticles. First-principles simulations reveal that the excellent catalytic performance of the single-atomic-site Ir on the defective metastable phase of titanium dioxide can be attributed to the appropriate strength of interactions between the active metal sites and the reactant molecules owing to the regulation of the supports.

KEYWORDS: single-atomic-site; metal-support interactions; biomass conversion; oxygen vacancy; selective hydrogenation

1. INTRODUCTION

Revealing the effect of metal–support interactions is one of the classic topics in heterogeneous catalysis.^{1–7} A large number of studies have shown that the supports not only play a role as anchors for dispersed metal catalysts, but can also affect or even modulate their catalytic properties.^{8–12} However, an in-depth investigation on the metal-support interactions is greatly hindered in most traditional metal catalysts due to the complicated compositions, configurations, and bonding patterns that are involved in the interactions. By contrast, single-atomic-site catalysts provide an ideal platform to explore the impact of such interactions on the catalytic performance of dispersed metal species, thanks to their simple structural features as well as recent advances in synthetic methods, characterization techniques, and computational simulations.^{13–22} Among the many developed methods of synthesizing single-atomic-site catalysts, such as co-precipitation¹³, impregnation¹⁶,

metal-organic framework encapsulation²³, polymer encapsulation²⁴, electrochemical strategy²⁵, to name a few, the central principle for designing stable single-atomic-site catalysts is to achieve strong interactions between isolate metal atoms and supporting materials.^{26–30} In turn, the metal-support interactions can be also used as an effective strategy to tune the catalytic properties of the deposited metal species.^{31–35} So far, however, very few works have been systematically performed to reveal the effects of metal-support interactions in regulating the performance of single-atomic-site catalysts.

As the chemical economy gradually shifts from fossil fuels to renewables, it is essential to develop technologies that can upgrade renewable platform molecules to industrially relevant products. Converting biomass and their derivatives to key chemicals has thus become a focus of academic research.^{36–39} Furfural, an important chemical platform derived from biomass feedstocks, serves as a versatile model compound for synthesizing multifunctional molecules.^{40–41} In its

transformation to furfural-derived chemicals and biofuels, selective hydrogenation is a commonly-used approach,⁴²⁻⁴⁷ through which, furfuryl alcohol can be produced for a broad applications in chemical industry. So far, the commercial production of furfuryl alcohol is mainly performed on copper chromite catalysts.⁴⁸ Despite the considerable achievements, the current process is subject to several disadvantages, including, harsh reaction conditions, high toxicity of the chromium trioxide and the deactivation of catalysts during the reactions, to name a few. It is thus highly desirable to explore an eco-friendly catalyst that can efficiently convert furfural to furfuryl alcohol under mild conditions. Various chromium-free catalysts containing noble or non-noble metal atoms have been developed.^{42-43,47,49-50} Typically, the noble metal-contained catalysts can exhibit better catalytic activity but suffer from the high cost of precious elements.

In this work, based on an exploration of metal-support interactions, we report the design and synthesis of a single-atomic-site Ir catalyst that can exhibit excellent performance toward biomass conversion. Herein, the Ir single atoms are placed on different supports of the defective metastable phase of titanium dioxide nanosheets ($\text{Ir}_1/\text{def-TiO}_2(\text{B})$) and the mesoporous graphitic carbon nitride samples ($\text{Ir}_1/\text{mpg-C}_3\text{N}_4$). The catalytic properties of Ir nanoparticles (~ 2 nm) are also investigated for the purpose of comparison. We find that the catalytic performance of the Ir species is regulated through changes in the geometric and electronic features. Among the three systems, the as-prepared $\text{Ir}_1/\text{def-TiO}_2(\text{B})$ catalyst exhibits outstanding conversion, high selectivity, and good stability in the hydrogenation of furfural to furfuryl alcohol, which are superior to $\text{Ir}_1/\text{mpg-C}_3\text{N}_4$ and the Ir nanoparticles. First-principles simulations reveal that the remarkable contrast in the catalytic properties is attributed to the different strength of interactions between Ir atoms and the reactant molecules owing to the regulation of the support materials.

2. EXPERIMENTAL SECTION

2.1 Catalyst preparation. Synthesis of the $\text{def-TiO}_2(\text{B})$, $\text{Ir}_1/\text{def-TiO}_2(\text{B})$ and the Ir nanoparticles catalysts. The $\text{def-TiO}_2(\text{B})$ was obtained through a reduction of the perfect metastable phase of titanium dioxide ($\text{per-TiO}_2(\text{B})$) at 250°C for 2 h in a 5% H_2/N_2 mixed atmosphere. In the typical synthesis of $\text{Ir}_1/\text{def-TiO}_2(\text{B})$, 500.0 mg $\text{def-TiO}_2(\text{B})$ was firstly dispersed in 100 mL water under ultrasonic vibration. The H_2IrCl_6 solution (2.5 mg H_2IrCl_6 in 10 mL water) was then dropwise added into the above solution under stirring at room temperature. After continuous stirring for about 24 h, the suspension was centrifuged. The recovered solid was washed with H_2O and methanol for one time and was finally dried in vacuum. The as-prepared powder was transferred into a ceramic boat and was then reduced at 200°C for 2 h in the 5% H_2/N_2 mixed atmosphere, in order to obtain the $\text{Ir}_1/\text{def-TiO}_2(\text{B})$ catalyst for further characterizations and catalysis tests. The Ir nanoparticles on $\text{def-TiO}_2(\text{B})$ was successfully synthesized using the same procedure, except that the mass of H_2IrCl_6 was increased to 62.5 mg. The content of Ir in Ir nanoparticles/ $\text{def-TiO}_2(\text{B})$ was estimated to be 2.40 wt%, as revealed by the

inductively coupled plasma optical emission spectrometry (ICP-OES) analysis.

Synthesis of $\text{Ir}_1/\text{mpg-C}_3\text{N}_4$. In the typical synthesis of $\text{Ir}_1/\text{C}_3\text{N}_4$, 250 mg $\text{mpg-C}_3\text{N}_4$ was dissolved in 50 mL water. The H_2IrCl_6 solution (1.5 mg H_2IrCl_6 in 5 mL water) was then added into the above solution under vigorous stirring. After continuous stirring for about 12h, the suspension was centrifuged. The recovered solid was washed with H_2O and methanol for one time and was finally dried in vacuum. The as-prepared powder was transferred into a ceramic boat, placed into a tube furnace, and was heated up to 150°C in N_2 atmosphere at a heating rate of 5°C min^{-1} . After that, the sample was treated at 150°C for 2 h. The loading of Ir, determined by the ICP-OES analysis, is 0.11 wt%.

2.2 Catalytic tests.

The hydrogenation of furfural was carried out in a 25 mL stainless steel autoclave with a pressure gauge, a magnetic stirrer and automatic temperature control apparatus. In the typical experiment, the reactant mixture that contains furfural (1 mmol), the catalyst {equal 0.0006 mmol Ir for $\text{Ir}_1/\text{def-TiO}_2(\text{B})$, $\text{Ir}_1/\text{mpg-C}_3\text{N}_4$ and Ir nanoparticles/ $\text{def-TiO}_2(\text{B})$ or 120 mg $\text{def-TiO}_2(\text{B})$ } and isopropanol (10 mL) were loaded into the reactor. The reactor was sealed, purged for three times with N_2 at 1 MPa, and was pressurized with 1 MPa H_2 and 3 MPa N_2 to a setting point. The reactor was then heated to 140°C and the stirring speed was fixed to 1000 rpm, in order to eliminate the diffusion effect. After 6 hours, the autoclave was cooled down quickly to stop the reactions. The autoclave contents were transferred to a centrifuge tube and were centrifuged to separate the catalyst.

During the stability test, the catalysts were reused without any further treatments. More specifically, during the hydrogenation reaction, the reaction mixture was centrifuged to recover the catalyst. The catalyst was first washed with acetone then with water followed by being dried in the vacuum oven at 50°C . After that, the catalyst was employed for the next catalytic test.

2.3 Computational details. Spin-polarized density functional theory calculations were performed using the Vienna *ab initio* simulation package (VASP).^{51,52} The projector augmented wave (PAW) approach⁵³ was employed, and the energy cutoff of the plane-wave basis set was set to 500 eV. The exchange-correlation interactions were described by the optB86b-vdW functional,^{54,55} which explicitly includes effects of van der Waals forces. The optimized lattice constants of the $\text{TiO}_2(\text{B})$ bulk ($a = 12.275 \text{ \AA}$, $b = 3.770$, $c = 6.592 \text{ \AA}$, and $\beta = 107.0^\circ$) agree very well with experiments⁵⁶ and previous calculations.^{57,58} For studying the formation of oxygen vacancies as well as the adsorption of an Ir single atom at the different vacancy sites, a symmetric 9-layer double-sided slab model was employed to simulate the $\text{TiO}_2(\text{B})$ (010)- 1×1 surface. Here, the first Brillouin zone was sampled using a $5 \times 3 \times 1$ Monkhorst-Pack grid.⁵⁹ In the calculations of the adsorption and reaction of the furfural reactants, a 5-layer single-sided slab model, as well as a 2×1 supercell, was used, and the Brillouin zone was sampled with a $2 \times 2 \times 1$ grid. To simulate the $\text{mpg-C}_3\text{N}_4$

sample and the Ir nanoparticles, a graphitic carbon nitride ($g\text{-C}_3\text{N}_4$) monolayer and an icosahedral Ir_{147} cluster model were employed, respectively. Structural relaxations were performed until the maximum residual force on each atom was less than 0.03 eV/\AA . Transition states were located using the climbing-image nudged elastic band method⁶⁰ and the dimer method⁶¹ with a force criterion of 0.05 eV/\AA . The energy barriers in the step of the associative desorption, however, were estimated using constrained optimization approach. Here, the vertical coordinate the sp^3 -type carbon atom was fixed, and the potential energy surfaces for furfuryl alcohol desorption were scanned accordingly. A dipole correction to the total energies was applied along the vertical direction.

3. RESULTS AND DISCUSSION

3.1. Characterizations of the single-atomic-site Ir samples. In the preparation of the $\text{Ir}_1/\text{def-TiO}_2(\text{B})$ material, the polymorphs $\text{per-TiO}_2(\text{B})$ nanosheets were firstly synthesized via hydrolyzing of titanium tetrachloride (TiCl_4) in ethylene glycol by using an existing scheme with minor modifications.⁶² After that, the $\text{per-TiO}_2(\text{B})$ nanosheets were thermally reduced under a hydrogen atmosphere, producing the polymorphs $\text{def-TiO}_2(\text{B})$ nanosheets that contain oxygen vacancies (for more details, see *experimental section*).⁶³ The transmission electron microscopy (TEM) images in Figure S1 clearly display a uniform morphology of the as-synthesized $\text{per-TiO}_2(\text{B})$ nanosheets. The phase compositions of the nanosheets were then characterized by X-ray diffraction (XRD). The obtained diffraction pattern corresponds to that of a metastable polymorph $\text{TiO}_2(\text{B})$ material (JCPDS 74-1940) and are different from those of the anatase and rutile TiO_2 structures (Figure S2). It is worth noting that upon the introduction of the oxygen vacancies, the original XRD pattern of $\text{per-TiO}_2(\text{B})$ remained in the $\text{def-TiO}_2(\text{B})$ nanosheets (Figure S2), meaning that the phase composition of the material did not change.

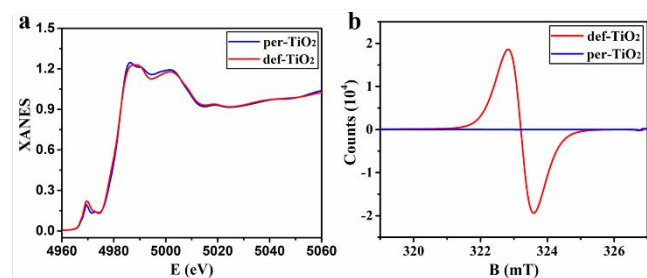


Figure 1. X-ray absorption analysis of Ti L_3 -edge and electron paramagnetic resonance (EPR) analysis. (a) XANES spectra of the Ti L_3 -edge for both per-TiO_2 and def-TiO_2 samples. (b) EPR analysis of per-TiO_2 and def-TiO_2 .

The X-ray absorption fine structure (XAFS) spectroscopy was utilized to probe the structure feature and the coordination environment of the $\text{def-TiO}_2(\text{B})$ substrates.⁶⁴ Here, both the $\text{per-TiO}_2(\text{B})$ and the $\text{def-TiO}_2(\text{B})$ samples (before Ir deposition) were investigated by the Ti K-edge X-ray absorption near-edge spectroscopy (XANES), with the normalized spectra resolved in Figure 1a. In the Ti K-preedge region, the preedge intensity of $\text{def-TiO}_2(\text{B})$ is higher than that of the $\text{per-TiO}_2(\text{B})$ nanosheets.

The contrast in the intensity reflects that the local coordination environments of the Ti atoms in $\text{def-TiO}_2(\text{B})$ is more noncentrosymmetric than those in $\text{per-TiO}_2(\text{B})$,⁶⁵ indicating the presence of oxygen point defects. The existence of the oxygen vacancies was further confirmed by the electron paramagnetic resonance (EPR) measurement. As shown in Figure 1b, pristine $\text{per-TiO}_2(\text{B})$ has no signal at room temperature, whereas the defective $\text{def-TiO}_2(\text{B})$ sample exhibits a remarkably strong EPR signal at $g = 2.003$, which originates from the oxygen vacancies according to previous literature.^{66,67}

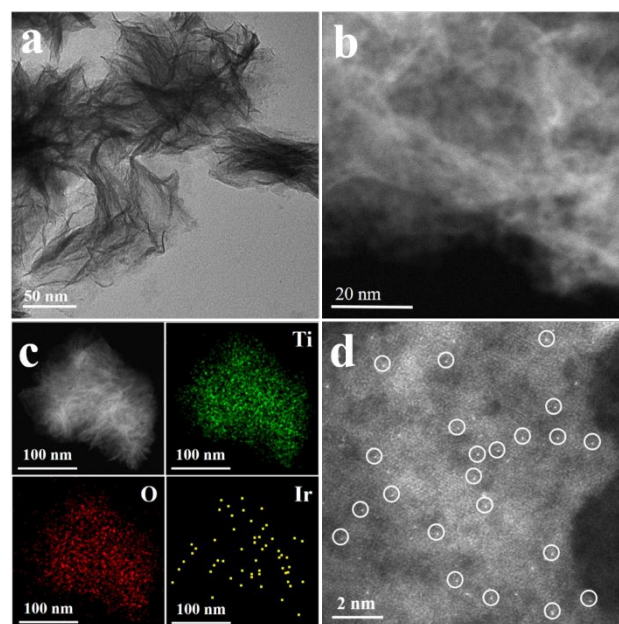


Figure 2. Characterization of $\text{Ir}_1/\text{def-TiO}_2(\text{B})$. (a) TEM image of the $\text{Ir}_1/\text{def-TiO}_2(\text{B})$ nanosheets. (b) HAADF-STEM image of a $\text{Ir}_1/\text{def-TiO}_2(\text{B})$ nanosheet. (c) EDX elemental mapping analysis for the distributions of Ti (blue), O (red), and Ir (green), respectively. (d) AC HAADF-STEM image of the $\text{Ir}_1/\text{def-TiO}_2(\text{B})$ sample.

We then employed the as-synthesized $\text{def-TiO}_2(\text{B})$ nanosheets as the support material for the deposition of Ir single atoms. Hexachloroiridium acid (H_2IrCl_6) was added into the water that contains well dispersed $\text{def-TiO}_2(\text{B})$ nanosheets. The mixture was then centrifuged, and the recovered solid was reduced in a hydrogen atmosphere, through which the $\text{Ir}_1/\text{def-TiO}_2(\text{B})$ catalyst was produced (for more details, see *experimental section*). The content of Ir was estimated to be 0.10 wt%, as revealed by the inductively coupled plasma optical emission spectrometry (ICP-OES) analysis. According to the TEM image (Figure 2a) and the high-angle annular dark-field scanning transmission electron microscope (HAADF-STEM) (Figure 2b) detection, there is no Ir nanoclusters or nanoparticles on the $\text{def-TiO}_2(\text{B})$ substrate. Besides, the XRD pattern did not exhibit any diffraction peaks of the Ir lattice either. The energy-dispersive X-ray (EDX) elemental mapping analysis confirmed that the Ir species are evenly dispersed on the $\text{def-TiO}_2(\text{B})$ nanosheets (Figure 2c). The characteristic of such Ir species was further elucidated by the aberration-

corrected HAADF-STEM (AC HAADF-STEM) measurements. Here, the atomically resolved AC HAADF-STEM image showed many small bright dots that are homogeneously distributed on the def-TiO₂(B) substrate. Since there is a remarkable difference between Ir, Ti and O elements in the Z-contrast⁴⁸, these small bright dots are determined as isolated single Ir atoms (Figure 2d).

Using the same procedure for the production of Ir₁/def-TiO₂(B) except the replacement of the substrate by mpg-C₃N₄ and a few minor changes in the pyrolysis conditions (for more details, see *experimental section*), the Ir₁/mpg-C₃N₄ samples were successfully synthesized. The loading of Ir is 0.11 wt% as determined by the ICP-OES analysis. According to the TEM and the HAADF-STEM images (Figures S3-5), there is no Ir nanoparticles nor nanoclusters, and the single Ir atoms were found to be homogeneously distributed on the mpg-C₃N₄ substrate. Such homogeneous distribution of the Ir species was further confirmed by the analysis of the EDX mapping. The above results demonstrate that the Ir species on mpg-C₃N₄ also exist as isolated single atoms.

The characteristic of the Ir species upon deposition was also investigated by XAFS studies. In Figure 3a, we present the Ir L₃-edge XANES spectra of the Ir₁/def-TiO₂(B) and the Ir₁/mpg-C₃N₄ samples as well as those of Ir powder and IrO₂ for comparison. It can be seen that the Ir₁ species on def-TiO₂(B) and mpg-C₃N₄ are both oxidized, with the carried positive charges being different from each other. These charge states of the single-atomic-site Ir species were further investigated by X-ray photoelectron spectroscopy (XPS), as shown in Figure S6. For Ir₁/def-TiO₂(B), the spectra are decomposed into three peaks, corresponding to the Ir 4f_{7/2}, Ir 4f_{5/2} and the Ti 3s levels. The binding energies of the Ir 4f_{7/2} level are 61.96 eV and 61.54 eV, respectively, for the Ir₁/def-TiO₂(B) and Ir₁/mpg-C₃N₄ samples, indicating that both Ir₁ species are oxidized but carry different positive charges (Figures S6-7). The results demonstrate that the charge states of the deposited Ir single atoms are indeed affected, but in varying degrees, by the metal-support interactions. The Fourier-transformed (FT) k³-weighted extended X-ray absorption fine structure (EXAFS) spectra of Ir₁/def-TiO₂(B) and Ir₁/mpg-C₃N₄ are shown in Figure 3b. It can be seen that for the Ir₁/def-TiO₂(B) sample, one Ir–O shell (*R* ~ 1.7 Å) is observed whereas contributions from Ir–Ir (*R* ~ 2.6 Å) bonds do not appear. The same results remain in the spectrum of Ir₁/mpg-C₃N₄, which merely includes peaks corresponding to the Ir–N/O shells. Interestingly, a second peak at a high *R* value (~ 2.4 Å) was found in the Ir₁/def-TiO₂(B) spectrum, which did not appear in that of Ir₁/mpg-C₃N₄. It reveals that on def-TiO₂(B), the Ir–Ti path should be taken into account as surrounding coordination environment for the Ir species. Thus, EXAFS analysis was further performed to extract detailed information on this issue. According to the fitting results, the average coordination numbers of Ir–O and Ir–Ti in Ir₁/def-TiO₂(B) are 3.2 and 2.8, respectively (Figures 3c-d, S8-11 and Table S1), while the average coordination numbers of the Ir–N/O bonds in Ir₁/mpg-C₃N₄ is 3.8 (Figures S12-13 and Table S1). The results demonstrate that the single-atomic-site Ir species are endowed with distinct geometric features by the metal-support interactions upon deposited on different supports.

The structure of the single-atomic-site Ir₁ species was further revealed by first-principles calculations. For the Ir₁/def-TiO₂(B) system, the (010) orientation of TiO₂(B) was adopted in the simulation of the substrate, since such type of surface was preferentially exposed in experiments.⁶² As shown in Figure S14, four nonequivalent oxygen atoms, *i.e.*, two 2-fold coordinated and two 3-fold coordinated ones, exist at the outermost layer of the (010) surface, corresponding to four types of oxygen vacancies. We systematically investigated the adsorption of an Ir single atom at the four vacancy sites and found that one configuration, in which the Ir atom is bonded to three Ti atoms, is energetically most favorable (Table S3). Once exposed to air, as in the XAFS experiments, the single-atomic-site Ir species can adsorb and dissociate one O₂ molecule, with its local structure shown in the inset of Figure 3c. Here, the numbers of the Ir–Ti and Ir–O bonds are both 3, consistent with results from the XAFS spectra. It should be noted that such configuration is different from the one upon being placed in a reducing H₂ atmosphere, where the adsorbed O species can be removed at the initial stage of hydrogenation reactions (the same for Ir₁/mpg-C₃N₄ in the reducing atmosphere). Regarding the Ir₁/mpg-C₃N₄ system, a graphitic carbon nitride (g-C₃N₄) monolayer was employed to simulate the framework. A single Ir atom is located at the sixfold cavity of mpg-C₃N₄, bonding with two N atoms. Once exposed to the air, an O₂ molecule can adsorb on the Ir single atom, with the configuration shown in Figure S12. The coordination number of the Ir atom is 4, corresponding to two Ir–N and two Ir–O bonds, also agreeing well with the XAFS results. Bader charge analysis revealed that both Ir species are oxidized, and the positive charge carried by Ir₁ on the def-TiO₂(B) support (1.01) is larger than that on the mpg-C₃N₄ monolayer (0.78). We note in passing that the value of Bader charges is not the same as, and in fact usually much smaller than that of the actual oxidation states.⁶⁸ The information from the DFT calculations is consistent with results from the XAFS and the XPS spectra.

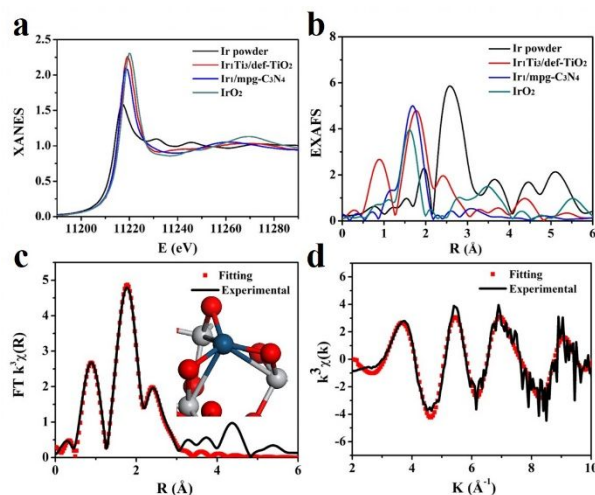


Figure 3. X-ray absorption analysis. (a) XANES spectra at the Ir L₃-edge of the Ir power, Ir₁/def-TiO₂(B), Ir₁/mpg-C₃N₄, and the IrO₂ samples, respectively. (b) Fourier transform (FT) at the Ir L₃-edge of the above four materials. (c, d) Corresponding fits of the EXAFS spectrum of Ir₁/def-TiO₂(B) at the *R* space and the *k* space, respectively, (black line: experimental data; red dot: fitting data).

The inset of panel c shows the local structure of the Ir₁ species on def-TiO₂(B) obtained from the DFT simulations.

3.2. Catalytic behaviors of the single-atomic-site Ir catalysts. The catalytic performance of the as-prepared single-atomic-site Ir samples was investigated for the selective hydrogenation of furfural. It is interesting to find that the Ir₁/def-TiO₂(B) catalyst displayed extremely high activity and selectivity in the production of furfuryl alcohol. Under a hydrogen pressure of 1 MPa and at 140°C, the attained conversion was as high as 99%, while no by-product, like tetrahydrofurfural, tetrahydrofurfuryl alcohol, furan, tetrahydrofuran, or levulinic acid product, was detected according to the gas chromatography-mass spectrometer (GC-MS) analysis. By comparing with the performance of the reported catalysts in previous works (listed in Table S2), we find that the Ir₁/def-TiO₂(B) catalyst in this work exhibits one of the best performance for the selective hydrogenation of furfural to furfuryl alcohol. In terms of the stability, the catalyst can be reused at least five times without any loss of the activity or the selectivity (Figure 4b). From the STEM and the AC HAADF-STEM characterizations, we did not find changes in the morphology of the samples, further supporting the robustness of the Ir₁/def-TiO₂(B) catalysts (Figure S15-16). We confirm that the catalytic effects of Ir₁/def-TiO₂(B) come from the Ir species, since the def-TiO₂(B) substrate is nearly inert under the same condition. For the Ir₁/mpg-C₃N₄ sample, only trace amounts of the furfuryl alcohol product were obtained, demonstrating that the catalytic performance of the single-atomic-site Ir species can indeed be influenced by the metal-support interactions. In addition, we have also examined the catalytic properties of Ir nanoparticles (ca. 2 nm, Figure S17). Similarly, the conversion sharply dropped, being only 8% of the value when using Ir₁/def-TiO₂(B) as the catalyst (Figure 4a).

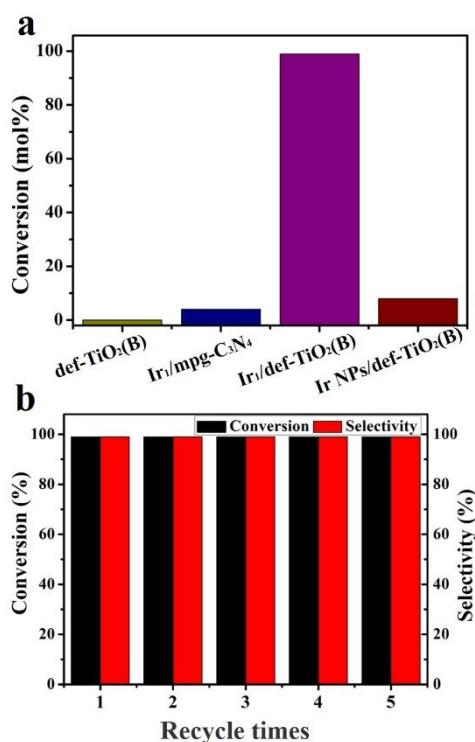


Figure 4. Catalytic performance for the selective hydrogenation of furfural to furfuryl alcohol. (a) The catalytic conversion of the different samples. (b) Recycle time of the Ir₁/def-TiO₂(B) catalyst.

3.3 First-principles calculations. The superior catalytic performance of Ir₁/def-TiO₂(B) compared with Ir₁/mpg-C₃N₄ and Ir nanoparticles can be attributed to an appropriate strength of interactions with the reactant molecules. For transition metal catalysts, the catalytic activity is determined by the strength of their interactions with the reactant molecules: Too weak interaction usually corresponds to a high reaction barrier, whereas too strong interaction makes products difficult to desorb, both of which impair the catalytic properties. As such, it is the intermediate interaction strength that brings about improved catalytic performance.^{69,70} According to our first-principles calculations the adsorption energies of furfural on the three Ir species are quite different, being 0.60 eV on Ir₁/mpg-C₃N₄, 1.63 eV on Ir₁/def-TiO₂(B), and 3.41 eV on the Ir₁₄₇ nanoparticle, respectively. As discussed below, the adsorption on Ir₁/mpg-C₃N₄ corresponds to the case where the interaction is too weak, whereas the adsorption on the Ir₁₄₇ nanoparticles corresponds to the case where the interaction is too strong. Thereby, it is the Ir₁/def-TiO₂(B) sample which exhibits the best catalytic performance.

The distinct contrast in the adsorption energies comes from an combined effect of both the electronic and the geometric factors. In Figure S18, we present the calculated projected density of state (PDOS) of the three Ir species. One can see that from Ir₁/mpg-C₃N₄ to Ir₁/def-TiO₂(B) and then to the Ir₁₄₇ nanoparticle, the DOS of the *d* electrons becomes more and more delocalized in the energy space. It makes the Ir species be able to interact with more number of discrete molecular levels (Figure S19), resulting in larger adsorption energies. Regarding the geometric factor, we present in Figure 5 the adsorption configurations of a furfural molecule on Ir₁/mpg-C₃N₄, Ir₁/def-TiO₂(B), and the Ir₁₄₇ nanoparticle. One can see that on mpg-C₃N₄, the Ir single atom locates within the plane of the monolayer, while other atoms around do not participate in the formation of chemical bonds with furfural. When being placed on the def-TiO₂(B) substrate, by contrast, the Ir single atom locates at a kink site, and an adjacent Ti atom also participates in the binding with the furfural molecule, both of which cause the increase in the adsorption energy. On the Ir₁₄₇ nanoparticle, at least four Ir atoms are directly involved in the formation of the chemical bonds, resulting in the strongest interaction. Due to the combined effects of the two factors, on Ir₁/mpg-C₃N₄, the furfural adsorbate is about 3.5 Å away from the Ir species, corresponding to a too weak interaction that makes Ir₁/mpg-C₃N₄ hardly play a role as a catalyst. On the Ir nanoparticle, both the furan ring and the carbonyl group interact with the Ir atoms, resulting in an over-strong interaction that makes the products difficult to desorb. The intermediate states could not effectively adjust their configurations during the reaction process either, which also impairs the catalytic properties. At the Ir₁ site on def-TiO₂(B), only the carbonyl group interacts with the substrate (in the middle panel in Figure S18), which results in the much-reduced adsorption energy compared to that on the Ir₁₄₇ nanoparticle. Besides, the simple bonding pattern is expected to facilitate the configuration adjustments of the intermediates states during the catalytic reaction. Thus, it is not surprising that Ir₁/def-TiO₂(B) exhibits much better catalytic

performance than the Ir₁/mpg-C₃N₄ sample and the Ir nanoparticles.

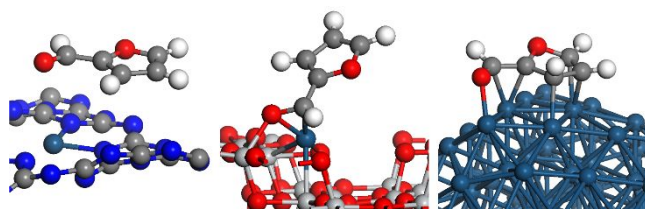


Figure 5. Adsorption configurations of a furfural molecule on the Ir₁/mpg-C₃N₄ monolayer (left), the Ir₁/def-TiO₂(B) substrate (middle), and the Ir₁₄₇ nanoparticle (right).

In Figure 6, we present the energy profile and the reaction pathway for the catalytic hydrogenation of furfural to furfuryl alcohol at the Ir₁ active site on def-TiO₂(B). Here, the adsorption of the furfural reactant and the H₂ molecule successively takes place, making the energy of the system reduced by 1.63 eV and 1.28 eV, respectively. It is worth noting that upon the adsorption, the H₂ molecule is highly activated, with its bond length increased from 0.75 Å to 1.08 Å. After that, the two hydrogen atoms react with furfural in a step-wise way, *i.e.*, transferring towards the aldehyde group one after the other. As such, the first hydrogen atom can bond with the carbon (green line) or the oxygen (blue line) atom of the aldehyde group, both of which were taken into account in the calculations. It was found that the former one is kinetically more favorable, since this pathway corresponds to a lower energy barrier in the second step. When both hydrogen atoms react with furfural, the produced furfuryl alcohol molecule weakly bonds with the substrate, mainly via van der Waals interactions, resulting in an easy desorption process.

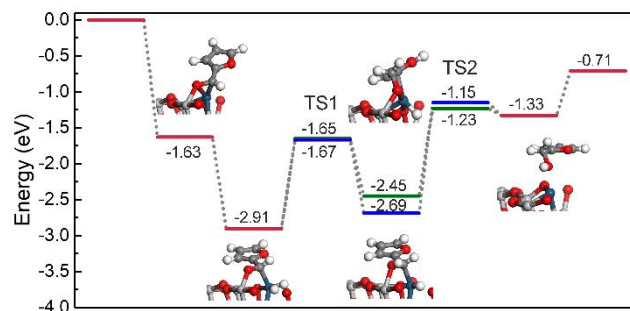


Figure 6. Energy profile (unit: eV) and reaction pathway for the catalytic hydrogenation of furfural to furfuryl alcohol at the Ir₁ active site on def-TiO₂(B). Structures of all the intermediate states are also shown on the energy profile.

4. CONCLUSION

In summary, the effects of metal-support interactions on the catalytic properties of the single-atomic-site catalysts are systematically investigated by considering two different substrates: def-TiO₂(B) and mpg-C₃N₄. The regulation on the geometric and electronic features of the Ir₁ species by the metal-support interactions has been revealed through advanced characterization techniques and first-principles simulations. Interestingly, Ir₁/def-TiO₂(B) exhibit excellent catalytic

performance in the selective hydrogenation of furfural to furfuryl alcohol, which is originated from an appropriate strength of the interactions with the reactant molecules. The Ir₁/def-TiO₂(B) catalyst also maintains satisfactory activity and selectivity in the reactions as verified by reusability tests. This work demonstrates that the properties of single-atomic-site catalysts can be modulated by metal-support interactions, and such a strategy could be used as an effective approach to design novel catalysts with superior catalytic performance.

ASSOCIATED CONTENT

AUTHOR INFORMATION

Corresponding Author

*qfu@sdu.edu.cn

*wangdingsheng@mail.tsinghua.edu.cn

ORCID

Qiang Fu: 0000-0002-6682-8527

Jun Luo: 0000-0001-5084-2087

Dingsheng Wang: 0000-0003-0074-7633

Yadong Li: 0000-0003-1544-1127

Author Contributions

*S.T., and W.G. contributed equally.

Notes

The authors declare no competing financial interests.

Supporting Information

The Supporting Information is available free of charge via the Internet at <http://pubs.acs.org>.

Detailed experimental procedures, characterization methods; TEM, HRTEM, and STEM images, Catalytic tests, EXAFS fitting curves (PDF).

ACKNOWLEDGMENT

This work was supported by the National Key R&D Program of China (2016YFA0202801), the National Natural Science Foundation of China (21890383, 21671117, 21871159, 21573129, 21803036). Q.F. also thanks supports from Shandong Provincial Natural Science Foundation, China (ZR2018QB005) and the Young Scholars Program of Shandong University (2018WLJH49). This work made use of the resources support of Beijing and Heifei National Synchrotron Radiation Laboratory. Theoretical calculations in this work were performed on the HPC Cloud Platform of Shandong University.

REFERENCES

- (1) Tauster, S. J.; Fung, S. C.; Garten, R. L. Strong Metal-Support Interactions. Group 8 Noble Metals Supported on TiO₂. *J. Am. Chem. Soc.* **1978**, *100*, 170–175.
- (2) Cargnello, M.; Delgado Jaen, J. J.; Hernandez Garrido, J. C.; Bakhmutsky, K.; Montini, T.; Calvino Gamez, J. J.; Gorte, R. J.; Fornasiero, P. Exceptional activity for methane combustion over modular Pd@CeO₂ subunits on functionalized Al₂O₃. *Science* **2012**, *337*, 713–717.
- (3) Cargnello, M.; Doan-Nguyen, V. V.; Gordon, T. R.; Diaz, R. E.; Stach, E. A.; Gorte, R. J.; Fornasiero, P.; Murray, C. B. Control of metal nanocrystal size reveals metal-support interface role for ceria catalysts. *Science* **2013**, *341*, 771–773.

- (4) Li, S.; Gong, J. Strategies for improving the performance and stability of Ni-based catalysts for reforming reactions. *Chem. Soc. Rev.* **2014**, *43*, 7245-7256.
- (5) Carrasco, J.; Lopez-Duran, D.; Liu, Z.; Duchon, T.; Evans, J.; Senanayake, S. D.; Crumlin, E. J.; Matolin, V.; Rodriguez, J. A.; Veronica Ganduglia-Pirovano, M. In Situ and Theoretical Studies for the Dissociation of Water on an Active Ni/CeO₂ Catalyst: Importance of Strong Metal-Support Interactions for the Cleavage of O-H Bonds. *Angew. Chem. Int. Ed.* **2015**, *54*, 3917-3921.
- (6) Matsubu, J. C.; Zhang, S.; DeRita, L.; Marinkovic, N. S.; Chen, J. G.; Graham, G. W.; Pan, X.; Christopher, P. Adsorbate-mediated strong metal-support interactions in oxide-supported Rh catalysts. *Nat. Chem.* **2017**, *9*, 120-127.
- (7) Dong, J.; Fu, Q.; Jiang, Z.; Mei, B.; Bao, X. Carbide-Supported Au Catalysts for Water-Gas Shift Reactions: A New Territory for the Strong Metal-Support Interaction Effect. *J. Am. Chem. Soc.* **2018**, *140*, 13808-13816.
- (8) Campbell, C. T. Catalyst-Support Interactions Electronic Perturbations. *Nat. Chem.* **2012**, *4*, 597-598.
- (9) Li, S.; Xu, Y.; Chen, Y.; Li, W.; Lin, L.; Li, M.; Deng, Y.; Wang, X.; Ge, B.; Yang, C.; Yao, S.; Xie, J.; Li, Y.; Liu, X.; Ma, D. Tuning the Selectivity of Catalytic Carbon Dioxide Hydrogenation over Iridium/Cerium Oxide Catalysts with a Strong Metal-Support Interaction. *Angew. Chem. Int. Ed.* **2017**, *56*, 10761-10765.
- (10) Zhu, W.; Wu, Z.; Foo, G. S.; Gao, X.; Zhou, M.; Liu, B.; Veith, G. M.; Wu, P.; Browning, K. L.; Lee, H. N.; Li, H.; Dai, S.; Zhu, H. Taming interfacial electronic properties of platinum nanoparticles on vacancy-abundant boron nitride nanosheets for enhanced catalysis. *Nat. Commun.* **2017**, *8*, 15291.
- (11) Zhao, E. W.; Zheng, H.; Ludden, K.; Xin, Y.; Hagelin-Weaver, H. E.; Bowers, C. R. Strong Metal-Support Interactions Enhance the Pairwise Selectivity of Parahydrogen Addition over Ir/TiO₂. *ACS Catal.* **2016**, *6*, 974-978.
- (12) Jackson, C.; Smith, G. T.; Inwood, D. W.; Leach, A. S.; Whalley, P. S.; Callisti, M.; Polcar, T.; Russell, A. E.; Leveque, P.; Kramer, D. Electronic metal-support interaction enhanced oxygen reduction activity and stability of boron carbide supported platinum. *Nat. Commun.* **2017**, *8*, 15802.
- (13) Qiao, B.; Wang, A.; Yang, X.; Allard, L. F.; Jiang, Z.; Cui, Y.; Liu, J.; Li, J.; Zhang, T. Single-atom catalysis of CO oxidation using Pt₁/FeOx. *Nat. Chem.* **2011**, *3*, 634-641.
- (14) Liu, P.; Zhao, Y.; Qin, R.; Mo, S.; Chen, G.; Gu, L.; Chevrier, D. M.; Zhang, P.; Guo, Q.; Zang, D.; Wu, B.; Fu, G.; Zheng, N. Photochemical route for synthesizing atomically dispersed palladium catalysts. *Science* **2016**, *352*, 797-801.
- (15) Nguyen, L.; Zhang, S.; Wang, L.; Li, Y.; Yoshida, H.; Patlolla, A.; Takeda, S.; Frenkel, A. I.; Tao, F. Reduction of Nitric Oxide with Hydrogen on Catalysts of Singly Dispersed Bimetallic Sites Pt₁Co_n and Pd₁Co_n. *ACS Catal.* **2016**, *6*, 840-850.
- (16) Shan, J.; Li, M.; Allard, L. F.; Lee, S.; Flytzani-Stephanopoulos, M. Mild oxidation of methane to methanol or acetic acid on supported isolated rhodium catalysts. *Nature* **2017**, *551*, 605-608.
- (17) Lin, J.; Wang, X. Rh single atom catalyst for direct conversion of methane to oxygenates. *Sci. China. Mater.* **2017**, *61*, 758-760.
- (18) Hu, M.; Zhang, J.; Zhu, W.; Chen, Z.; Gao, X.; Du, X.; Wan, J.; Zhou, K.; Chen, C.; Li, Y. 50 ppm of Pd dispersed on Ni(OH)₂ nanosheets catalyzing semi-hydrogenation of acetylene with high activity and selectivity. *Nano Res.* **2017**, *11*, 905-912.
- (19) Tian, S.; Wang, Z.; Gong, W.; Chen, W.; Feng, Q.; Xu, Q.; Chen, C.; Chen, C.; Peng, Q.; Gu, L.; Zhao, H.; Hu, P.; Wang, D.; Li, Y. Temperature-Controlled Selectivity of Hydrogenation and Hydrodeoxygenation in the Conversion of Biomass Molecule by the Ru₁/mpg-C₃N₄ Catalyst. *J. Am. Chem. Soc.* **2018**, *140*, 11161-11164.
- (20) Wang, A.; Li, J.; Zhang, T. Heterogeneous single-atom catalysis. *Nat. Rev. Chem.* **2018**, *2*, 65-81.
- (21) Chen, Y.; Ji, S.; Chen, C.; Peng, Q.; Wang, D.; Li, Y. Single-atom catalysts: Synthetic strategies and electrochemical applications. *Joule* **2018**, *2*, 1242-1264.
- (22) Zhu, Y.; Cao, T.; Cao, C.; Luo, J.; Chen, W.; Zheng, L.; Dong, J.; Zhang, J.; Han, Y.; Li, Z.; Chen, C.; Peng, Q.; Wang, D.; Li, Y. One-Pot Pyrolysis to N-Doped Graphene with High-Density Pt Single Atomic Sites as Heterogeneous Catalyst for Alkene Hydrosilylation. *ACS Catal.* **2018**, *8*, 10004-10011.
- (23) Chen, Y.; Ji, S.; Wang, Y.; Dong, J.; Chen, W.; Li, Z.; Shen, R.; Zheng, L.; Zhuang, Z.; Wang, D.; Li, Y. Isolated Single Iron Atoms Anchored on N-Doped Porous Carbon as an Efficient Electrocatalyst for the Oxygen Reduction Reaction. *Angew. Chem. Int. Ed.* **2017**, *56*, 6937-6941.
- (24) Zhang, M.; Wang, Y. G.; Chen, W.; Dong, J.; Zheng, L.; Luo, J.; Wan, J.; Tian, S.; Cheong, W. C.; Wang, D.; Li, Y. Metal (Hydr)oxides@Polymer Core-Shell Strategy to Metal Single-Atom Materials. *J. Am. Chem. Soc.* **2017**, *139*, 10976-10979.
- (25) Zhang, J.; Zhao, Y.; Guo, X.; Chen, C.; Dong, C.-L.; Liu, R.-S.; Han, C.-P.; Li, Y.; Gogotsi, Y.; Wang, G. Single platinum atoms immobilized on an MXene as an efficient catalyst for the hydrogen evolution reaction. *Nature Catalysis* **2018**, *1*, 985-992.
- (26) Chen, Z.; Mitchell, S.; Vorobyeva, E.; Leary, R. K.; Hauert, R.; Furnival, T.; Ramasse, Q. M.; Thomas, J. M.; Midgley, P. A.; Dontsova, D.; Antonietti, M.; Pogodin, S.; Lopez, N.; Perez-Ramirez, J. Stabilization of Single Metal Atoms on Graphitic Carbon Nitride. *Adv. Funct. Mater.* **2017**, *27*, 1605785.
- (27) O'Connor, N. J.; Jonayat, A. S. M.; Janik, M. J.; Senftle, T. P. Interaction trends between single metal atoms and oxide supports identified with density functional theory and statistical learning. *Nat. Catal.* **2018**, *1*, 531-539.
- (28) Lou, Y.; Wu, H.; Liu, J. Nanocarbon-Edge-Anchored High-Density Pt Atoms for 3-nitrostyrene Hydrogenation: Strong Metal-Carbon Interaction. *iScience* **2019**, *13*, 190-198.
- (29) Lang, R.; Xi, W.; Liu, J.-C.; Cui, Y.-T.; Li, T.; Lee, A. F.; Chen, F.; Chen, Y.; Li, L.; Li, L.; Lin, J.; Miao, S.; Liu, X.; Wang, A.-Q.; Wang, X.; Luo, J.; Qiao, B.; Li, J.; Zhang, T. Non defect-stabilized thermally stable single-atom catalyst. *Nat. Commun.* **2019**, *10*, 234.
- (30) Zhang, J.; Liu, C.; Zhang, B. Insights into Single-Atom Metal-Support Interactions in Electrocatalytic Water Splitting. *Small Methods* **2019**, 1800481.
- (31) Wang, L.; Li, H.; Zhang, W.; Zhao, X.; Qiu, J.; Li, A.; Zheng, X.; Hu, Z.; Si, R.; Zeng, J. Supported Rhodium Catalysts for Ammonia-Borane Hydrolysis: Dependence of the Catalytic Activity on the Highest Occupied State of the Single Rhodium Atoms. *Angew. Chem. Int. Ed.* **2017**, *56*, 4712-4718.
- (32) Guo, Y.; Mei, S.; Yuan, K.; Wang, D.-J.; Liu, H.-C.; Yan, C.-H.; Zhang, Y.-W. Low-Temperature CO₂ Methanation over CeO₂-Supported Ru Single Atoms, Nanoclusters, and Nanoparticles Competitively Tuned by Strong Metal-Support Interactions and H-Spillover Effect. *ACS Catal.* **2018**, *8*, 6203-6215.
- (33) Zhang, Q.; Qin, X.-X.; Duan-Mu, F.-P.; Ji, H.-M.; Shen, Z.-R.; Han, X.-P.; Hu, W.-B. Isolated Platinum Atoms Stabilized by Amorphous Tungstenic Acid: Metal-Support Interaction for Synergistic Oxygen Activation. *Angew. Chem. Int. Ed.* **2018**, *57*, 9351-9356.
- (34) Li, H.; Wang, M.; Luo, L.; Zeng, J. Static Regulation and Dynamic Evolution of Single-Atom Catalysts in Thermal Catalytic Reactions. *Adv. Sci.* **2019**, *6*, 1801471.
- (35) Zhou, P.; Lv, F.; Li, N.; Zhang, Y.; Mu, Z.; Tang, Y.; Lai, J.; Chao, Y.; Luo, M.; Lin, F.; Zhou, J.; Su, D.; Guo, S. Strengthening reactive metal-support interaction to stabilize high-density Pt single atoms on electron-deficient g-C₃N₄ for boosting photocatalytic H₂ production. *Nano Energy* **2019**, *56*, 127-137.
- (36) Huber, G. W.; Chheda, J. N.; Barrett, C. J.; Dumesic, J. A. Production of liquid alkanes by aqueous-phase processing of biomass-derived carbohydrates. *Science* **2005**, *308*, 1446-1450.

- (37) Besson, M.; Gallezot, P.; Pinel, C. Conversion of biomass into chemicals over metal catalysts. *Chem. Rev.* **2014**, *114*, 1827-1870.
- (38) Zhao, M.; Yuan, K.; Wang, Y.; Li, G.; Guo, J.; Gu, L.; Hu, W.; Zhao, H.; Tang, Z. Metal-organic frameworks as selectivity regulators for hydrogenation reactions. *Nature* **2016**, *539*, 76-80.
- (39) Motagamwala, A. H.; Won, W.; Sener, C.; Alonso, D. M.; Maravelias, C. T.; Dumesic, J. A. Toward biomass-derived renewable plastics: Production of 2,5-furandicarboxylic acid from fructose. *Sci. Adv.* **2018**, *4*, 9722.
- (40) Choudhary, V.; Mushrif, S. H.; Ho, C.; Anderko, A.; Nikolakis, V.; Marinkovic, N. S.; Frenkel, A. I.; Sandler, S. I.; Vlachos, D. G. Insights into the interplay of Lewis and Bronsted acid catalysts in glucose and fructose conversion to 5-(hydroxymethyl)furfural and levulinic acid in aqueous media. *J. Am. Chem. Soc.* **2013**, *135*, 3997-4006.
- (41) Mellmer, M. A.; Sener, C.; Gallo, J. M.; Luterbacher, J. S.; Alonso, D. M.; Dumesic, J. A. Solvent effects in acid-catalyzed biomass conversion reactions. *Angew. Chem. Int. Ed.* **2014**, *53*, 11872-11875.
- (42) Pang, S. H.; Schoenbaum, C. A.; Schwartz, D. K.; Medlin, J. W. Directing reaction pathways by catalyst active-site selection using self-assembled monolayers. *Nat. Commun.* **2013**, *4*, 2448.
- (43) Nakagawa, Y.; Takada, K.; Tamura, M.; Tomishige, K. Total Hydrogenation of Furfural and 5-Hydroxymethylfurfural over Supported Pd-Ir Alloy Catalyst. *Acs Catal.* **2014**, *4*, 2718-2726.
- (44) Mariscal, R.; Maireles-Torres, P.; Ojeda, M.; Sádaba, I.; López Granados, M. Furfural: a renewable and versatile platform molecule for the synthesis of chemicals and fuels. *Energ. Environ. Sci.* **2016**, *9*, 1144-1189.
- (45) Mironenko, A. V.; Vlachos, D. G. Conjugation-Driven "Reverse Mars-van Krevelen"-Type Radical Mechanism for Low-Temperature C-O Bond Activation. *J. Am. Chem. Soc.* **2016**, *138*, 8104-8113.
- (46) Taylor, M. J.; Durndell, L. J.; Isaacs, M. A.; Parlett, C. M. A.; Wilson, K.; Lee, A. F.; Kyriakou, G. Highly selective hydrogenation of furfural over supported Pt nanoparticles under mild conditions. *Appl. Catal. B-Environ.* **2016**, *180*, 580-585.
- (47) Gong, W.; Chen, C.; Zhang, Y.; Zhou, H.; Wang, H.; Zhang, H.; Zhang, Y.; Wang, G.; Zhao, H. Efficient Synthesis of Furfuryl Alcohol from H₂-Hydrogenation/Transfer Hydrogenation of Furfural Using Sulfonate Group Modified Cu Catalyst. *ACS Sustain. Chem. Eng.* **2017**, *5*, 2172-2180.
- (48) Rao, R.; Dandekar, A.; Baker, R. T. K.; Vannice, M. A. Properties of Copper Chromite Catalysts in Hydrogenation Reactions. *J. Catal.* **1997**, *171*, 406-419.
- (49) Zhang, H.; Gu, X. K.; Canlas, C.; Kropf, A. J.; Aich, P.; Greeley, J. P.; Elam, J. W.; Meyers, R. J.; Dumesic, J. A.; Stair, P. C.; Marshall, C. L. Atomic layer deposition overcoating: tuning catalyst selectivity for biomass conversion. *Angew. Chem. Int. Ed.* **2014**, *53*, 12132-12136.
- (50) Wang, C.; Wang, L.; Zhang, J.; Wang, H.; Lewis, J. P.; Xiao, F. S. Product Selectivity Controlled by Zeolite Crystals in Biomass Hydrogenation over a Palladium Catalyst. *J. Am. Chem. Soc.* **2016**, *138*, 7880-7883.
- (51) Kresse, G.; Furthmüller, J. Efficiency of ab-initio total energy calculations for metals and semiconductors using a plane-wave basis set. *Comput. Mater. Sci.* **1996**, *6*, 15-50.
- (52) Kresse, G.; Furthmüller, J. Efficient iterative schemes for ab initio total-energy calculations using a plane-wave basis set. *Phys. Rev. B* **1996**, *54*, 11169-11186.
- (53) Blöchl, P. E. The projector augmented wave method. *Phys. Rev. B* **1994**, *50*, 17953-17979.
- (54) Dion, M.; Rydberg, H.; Schröder, E.; Langreth, D. C.; Lundqvist, B. I. Van der Waals density functional for general geometries. *Phys. Rev. Lett.* **2004**, *92*, 246401.
- (55) Klimeš, J.; Bowler, D. R.; Michaelides, A. Chemical accuracy for the van der Waals density functional. *J. Phys.: Condens. Matter.* **2010**, *22*, 022201.
- (56) Feist, T. P.; Davies, P. K. The soft chemical synthesis of TiO₂(B) from layered titanates. *J. Solid State Chem.* **1992**, *101*, 275-295.
- (57) Ben Yahia, M.; Lemoigno, F.; Beuvier, T.; Filhol, J.-S.; Richard-Plouet, M.; Brohan, L.; Doublet, M.-L. Updated references for the structural, electronic, and vibrational properties of TiO₂(B) bulk using first-principles density functional theory calculations. *J. Chem. Phys.* **2009**, *130*, 204501.
- (58) Vittadini, A.; Casarin, M.; Selloni, A. Structure and Stability of TiO₂-B Surfaces: A Density Functional Study. *J. Phys. Chem. C* **2009**, *113*, 18973-18977.
- (59) Monkhorst, H. J.; Pack, J. D. Special points for Brillouin-zone integrations. *Phys. Rev. B* **1976**, *13*, 5188-5192.
- (60) Henkelman, G.; Uberuaga, B. P.; Jónsson, H. A climbing image nudged elastic band method for finding saddle points and minimum energy paths. *J. Chem. Phys.* **2000**, *113*, 9901-9904.
- (61) Henkelman, G.; Jónsson, H. A dimer method for finding saddle points on high dimensional potential surfaces using only first derivatives. *J. Chem. Phys.* **1999**, *111*, 7010-7022.
- (62) Xiang, G.; Li, T.; Zhuang, J.; Wang, X. Large-scale synthesis of metastable TiO₂(B) nanosheets with atomic thickness and their photocatalytic properties. *Chem. Commun.* **2010**, *46*, 6801-6803.
- (63) Chen, X.; Liu, L.; Yu, P. Y.; Mao, S. S. Increasing solar absorption for photocatalysis with black hydrogenated titanium dioxide nanocrystals. *Science* **2011**, *331*, 746-750.
- (64) Sun, Z.; Liu, Q.; Yao, T.; Yan, W.; Wei, S. X-ray absorption fine structure spectroscopy in nanomaterials. *Sci. China Mater.* **2015**, *58*, 313-341.
- (65) Kronawitter, C. X.; Bakke, J. R.; Wheeler, D. A.; Wang, W. C.; Chang, C.; Antoun, B. R.; Zhang, J. Z.; Guo, J.; Bent, S. F.; Mao, S. S.; Vayssieres, L. Electron enrichment in 3d transition metal oxide hetero-nanostructures. *Nano Lett.* **2011**, *11*, 3855-3861.
- (66) Zuo, F.; Wang, L.; Wu, T.; Zhang, Z.; Borchardt, D.; Feng, P. Self-doped Ti³⁺ enhanced photocatalyst for hydrogen production under visible light. *J. Am. Chem. Soc.* **2010**, *132*, 11856-11857.
- (67) Wang, S.; Pan, L.; Song, J. J.; Mi, W.; Zou, J. J.; Wang, L.; Zhang, X. Titanium-defected undoped anatase TiO₂ with p-type conductivity, room-temperature ferromagnetism, and remarkable photocatalytic performance. *J. Am. Chem. Soc.* **2015**, *137*, 2975-83.
- (68) Wang, B.; Li, S. L.; Truhlar, D. G. Modeling the partial atomic charges in inorganometallic molecules and solids and charge redistribution in lithium-ion cathodes. *J. Chem. Theory Comput.* **2014**, *10*, 5640-5650.
- (69) Nørskov, J. K.; Bligaard, T.; Rossmeisl, J. & Christensen, C. H. Towards the computational design of solid catalysts. *Nat. Chem.* **2009**, *1*, 37-46.
- (70) Nørskov, J. K.; Studt, F.; Abild-Pedersen, F. & Bligaard, T. Fundamental Concepts in Heterogeneous Catalysis; John Wiley & Sons, Inc.: Hoboken, NJ, 2014.

